Proton acceleration: experimental setup

The *Salle Jaune* experimental area at the *Laboratoire d'Optique Appliquée* contains a multi-terawatt, CPA based, laser chain and the experimental installation that is needed for ultra-high intensity experiments. This chapter is dedicated to a deeper insight on the setup that we realized for the acceleration and characterization of ion beams. The focusing quality of the laser beam influences the cutoff energies and the dynamics of the accelerated beam, which requires a careful alignment of the focusing optics (a parabola at $f/3$) and a precise control of the original laser beam. The large numerical aperture sets very small boundaries on the positioning of the target, whereas the main proton diagnostic (Thomson Parabola and Micro-Channel Plate) requires the tilt of the target to be lower than $1°$. The structure of the laser chain and the optical part of our experimental installation is here presented, from the focusing of the beam to the alignment of the target. A second part is dedicated to the ion diagnostics that have been put in place. The experimental results and their interpretation are presented in Ch.7.

6.1 The laser source

The *Salle Jaune* laser is a Titanium-Sapphire (Ti:Sa) solid state laser and belongs to the category of T^3 lasers (Table Top Terawatt). It is a multi-stage CPA chain composed by a pre-amplified front-end and three multipass amplifiers, capable of delivering up to $2J$ per pulse (before compression) at a repetition rate of $10Hz$. More in detail (see scheme in Fig.6.1):

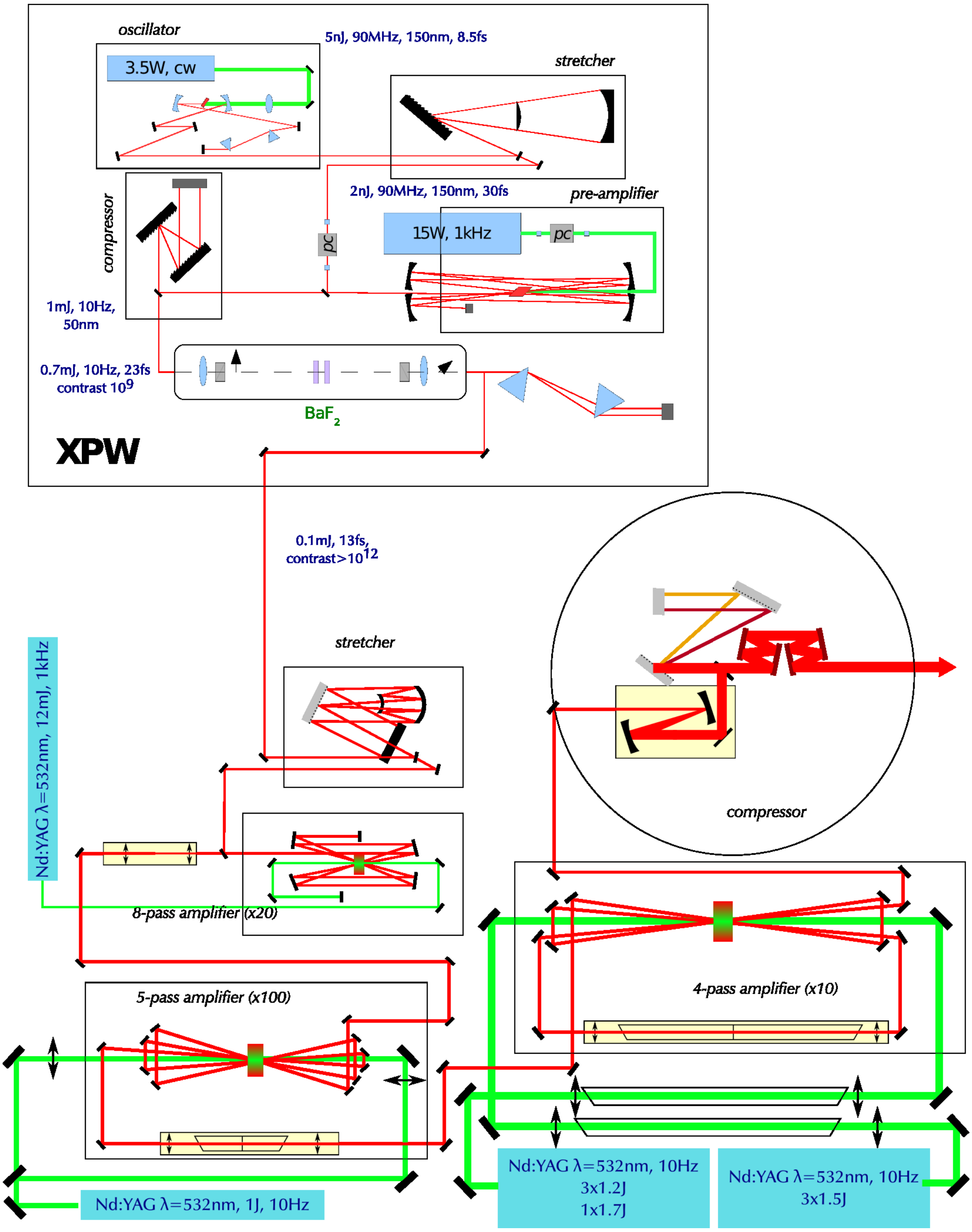

Figure 6.1: Block scheme of the *Salle Jaune* laser system.

Oscillator: a Ti:Sapphire, Kerr-lens mode-locked, oscillator produces a train of $8.5fs$ pulses, with a per-pulse energy of $5nJ$ at a repetition rate of $88MHz$. The central wavelength is $\lambda = 810nm$ and the spectrum is $150nm$ FWHM[1].

Preamplification and XPW: The repetition frequency from the oscillator is cut down to $10Hz$ by Pockels cells. The selected pulse is stretched, pre-amplified to $1mJ$ and compressed back to $23fs$, in order to be injected in the XPW system (see 6.1.1). The preamplifier is charged by a diode-pumped CW laser, which noticeably improves the stability.

Multipass amplification: the pulse is stretched to $600ps$ and injected in a three stages (4-pass, 5-pass and 3-pass) chain of Ti:Sa amplifiers pumped by doubled Nd:YAG lasers. The beam undergoes spatial filtering after each amplifier. The complete amplification process brings $100nJ$ (after XPW) to $\approx 2J$. The contrast worsen from 10^{12} to $10^9 \div 10^{10}$.

Separation of the beams: Before the compression, a partially reflecting mirror (in our experiment was 10%) is used to create a second beam (*probe*) with lower energy. A $\lambda/2$ filter and a polarizer cube are used to introduce a variable loss. Finally, a motorized delay line is provided to change the delay between the two beams.

Compression: The two beams of $400ps$ pulses are compressed by two separate grating compressors to a duration of approximately $30fs$ with an efficiency that ranges between 45% and $\approx$ 55%.

Phase front cleaning: the wave front of the *pump* beam is corrected by a cylindrical symmetry deformable mirror (see 6.2.1).

6.1.1 Enhancement of the Contrast

The contrast ratio (Fig.6.2) of an UHI pulse is a parameter of great importance when speaking of interaction with matter (Ch.3, 3.4). Many features, many of them not completely exploited, of the interaction process are correlated with the total energy and the over-threshold duration of the pedestal that precedes the main peak. From a CPA chain, three types of effects are in general observed.

[1]The effective spectrum width is lowered as the pulse undergoes the following amplifications. This is due to the non-linear gain in the crystals and to the non-constant gain envelope for different frequency components, which makes central wavelengths to be more amplified than peripheral ones.

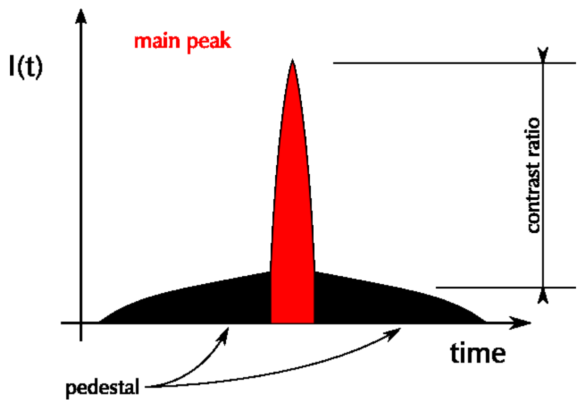

Figure 6.2: The contrast of a short pulse.

Prepulses Replica of the *fs* pulse can be produced, by various reasons, before and after the main pulse. Examples are *(i)* insufficient extinction power of the Pockels cell that selects the pulse from the oscillator, *(ii)* the presence of shortcuts in the optical path or *iii* cuts in the pulse spectrum.

Background light In the oscillator cavity, the production of *fs* pulses (with a repetition rate of $88MHz$ and a per-pulse energy of some nJ) is a process which is in competition with the continuous wave (CW) production, which results in a continuous background around the *fs* pulses. The contrast in the oscillator pulse train can however be as high as 10^9.

Amplified Spontaneous Emission The ASE comes from the spontaneous emission in charged crystals, which is produced before the passage of the main pulse. The ASE is amplified in the forthcoming crystals, worsening the contrast. The importance of the spontaneous emission is directly bound to the gain in the amplifiers and to the timing between the pump laser pulses (used to charge the mediums) and the seed laser pulse (to be amplified).

The path of the pulse in the optical system controlled by optical shutters (Pockels cells). Their synchrony to the pulse sets the mark on the prepulse structure, cutting the sum of the three effects to a well defined light front. In *Salle Jaune*, the Pockels cells cut the pedestal between $2.5ns$ and $3ns$ before the *fs* pulse. In the original chain, before any active contrast enhancement technique was adopted, the peak to pedestal ratio was, $I_{max}/I_{ASE} = 10^7$ from $3ns$ before, and $I_{max}/I_{pre-p} = 10^5$ for prepulses $100ps$ before (Fig.6.3-*(upper)*,[96]).

XPW

The use of **XPW** (acronym for *Crossed Polarized Wave generation*) to improve the contrast in a laser chain has been introduced at the *Laboratoire d'Optique Appliquée* [45, 47, 48] after previous studies [69, 70, 46] on the $\chi^{(3)}$ anisotropy of BaF_2 glasses. The generation of a crossed-polarized wave is a degenerate, $\omega \rightarrow \omega$, four wave mixing process, where a rotation of the polarization is produced between the input and the output wave. From [47] the equations for the non-linear propagation are written as

$$\begin{aligned} \frac{\mathrm{d}A}{\mathrm{d}z} &= \mathrm{i}\gamma_1|A|^2A - \mathrm{i}\gamma_2\left(|B|^2B - A^2B^* - 2|A|^2B\right) + \mathrm{i}\gamma_3\left(2|B|^2A + B^2A^*\right) \\ \frac{\mathrm{d}B}{\mathrm{d}z} &= \mathrm{i}\gamma_1|B|^2B - \mathrm{i}\gamma_2\left(|A|^2A - B^2A^* - 2B^2A\right) + \mathrm{i}\gamma_3\left(2|A|^2B + A^2B^*\right), \end{aligned} \tag{6.1}$$

where $A(z)$ ($A(0) = A_0$) is the input wave amplitude and $B(z)$ ($B(0) = 0$) is the cross-polarized wave; the factor $\gamma_{\{1,2,3\}}$ depends on the non-linear tensor of the material and the polarization angle.

The enhancement of contrast relies on the fact that the III-order non-linear process holds a 3^{rd} order dependency of the output field on the input field. This produces a rotation of the polarization which depends on the 3^{rd} power of the incoming intensity. The effect is optimized by matching the thickness of the BaF_2 crystals with the input amplitude A_0 from (6.1); two polarizers in the final setup are used to *(i)* set the input polarization, *(ii)* select the output. In [5] a contrast of 10^{12} is reported, from 3ω autocorrelation measurements on the *Salle Jaune* front-end.

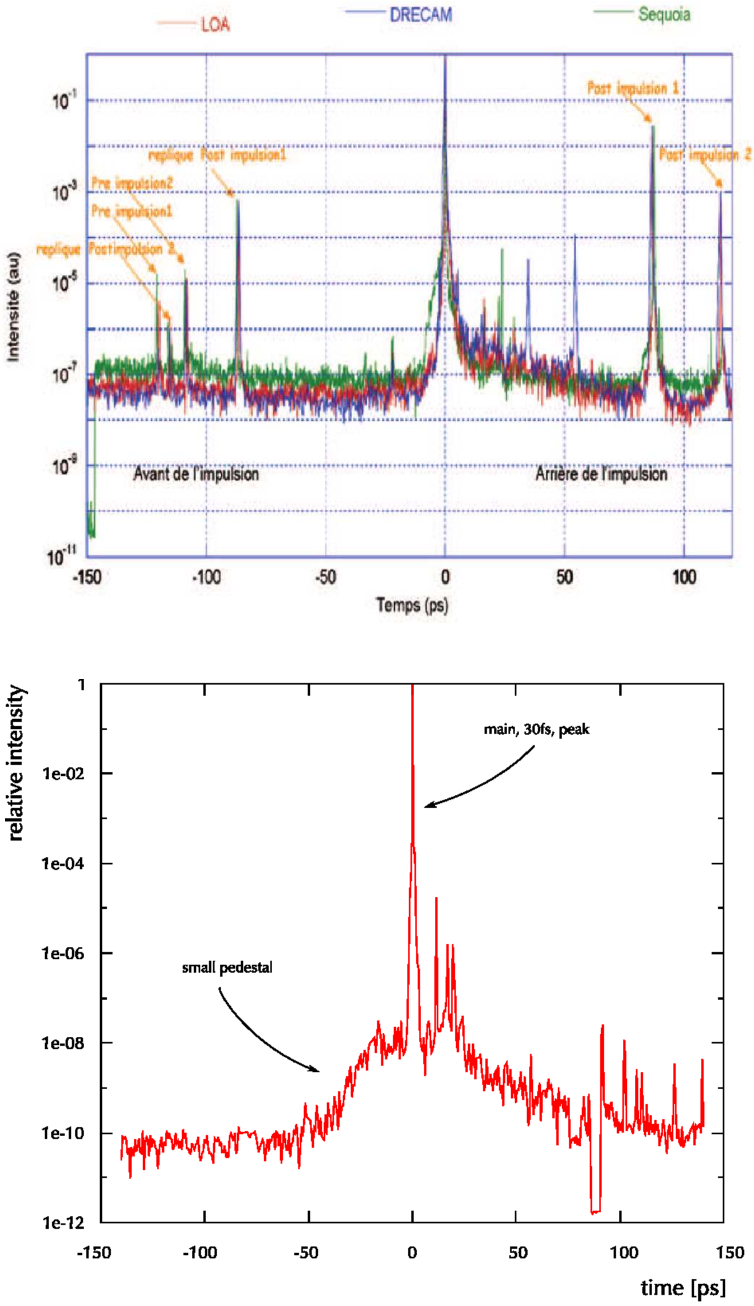

Figure 6.3: *(upper)* Contrast on the previous (up to year 2006) configuration of the *Salle Jaune* laser (excerpt from [96]); *(lower)* 3ω measure of present contrast, with a two crystals XPW system.

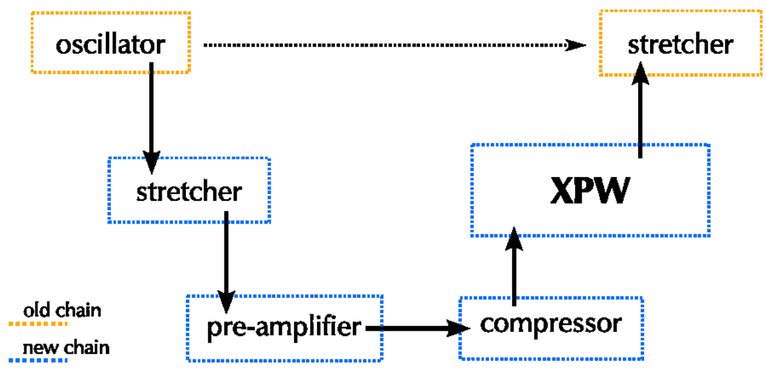

Figure 6.4: XPW system insertion on the laser chain (left), between the oscillator and the 8-pass amplifier, and picture of the setup (right)

The theoretical efficiency in terms of contrast enhancement is limited by the extinction power of the two polarizers (the polarizer before and the analyzer after) that are used to set the input polarization and select the cross-polarized output. The low generation efficiency (12% and 25% respectively for single or double crystal arrangement) and the necessity to work on the compressed pulse made necessary to pre-amplify the pulse (and compress it back) before entering the system (Fig.6.4).

Other systems Different solutions have been proposed to increase the contrast ratio in CPA chains; at present the most common and effectively used among the community of laser ion acceleration are fast Pockels cells and plasma mirrors. The firsts are Pockels cells with an improved high voltage power supply, with reduced rise and fall times, thus able to open and close the optical circuit in a faster way. They are used to directly cut the pedestal to a shorter duration before the *fs* peak. In CPA systems they are best used in the initial part of the chain, where higher gain produces faster contrast worsening and the laser intensity is lower, hence limiting the energy loss in the Pockels crystal. Typical response values are $300ps$ rise time and $150ps$ jitter.

Plasma mirrors use the pedestal energy to produce a plasma on a transparent slab of glass that in turns reflects the laser beam[17, 50, 37, 7]. The beam is focused to a level where the pedestal itself has sufficient energy to produce a supercritical, solid density, plasma. The peak intensity due to pedestal on the mirror have to be accurately calculated to avoid expansion of the plasma (early ionization) or transmission of a part of the main peak (late ionization). In the ideal case, the pedestal is transmitted or absorbed, while the peak is reflected: double plasma mirrors have been shown able to cut the pedestal to a contrast better than 10^{10}. Recent results [55] reported a total efficiency for the double mirror setup of $\approx 50\%$. Another drawback is that mirrors are damaged in the process and they have to be moved after after each shot.

It has to be underlined that the pulse, once cleaned by a plasma mirror, is qualitatively different from what is obtained by XPW; this fact will be taken in account when comparing our data to proton spectra from literature.

6.1.2 Adaptive correction of the phase front

The extent the beam can be focus to, meaning the ability to concentrate the biggest part of energy into a spot as small as possible, depends on the quality of the beam's transverse profile. On a beam from a CPA is often present a certain level of distortion, due to the number of refractive optics on its path and the non perfectly uniform effect of crystals, including thermal lensing effects and non completely isotropic pumping.

On the *Salle Jaune* laser system, a deformable mirror is used to partially correct the

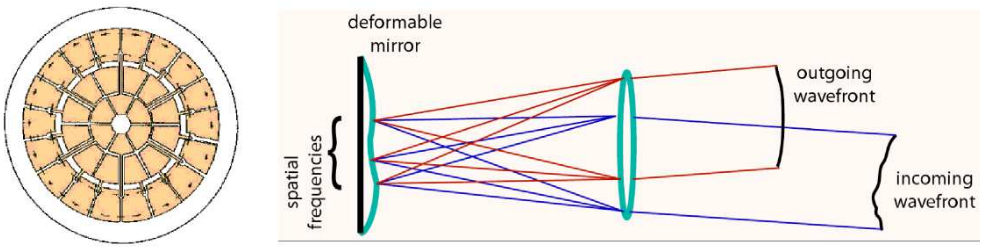

Figure 6.5: Deformable mirror: the mirror surface is on the focal plane of a lens, where the spatial frequencies of the phase surface are mapped.

beam wave front, so the quality of the focused spot. It is composed by 52 bi-morph actuators in cylindrical symmetry, which can correct up to the 6^{th} order of aberration in Zernike polynomials. The correction procedure is accomplished in two steps.

In the first step a self-learning loop builds the matrix of correlation between the movement of actuators and the projection of the phase surface – after the mirror– on the space of Zernike polynomials[2]. The correction matrix depends on the beam characteristics, so that the procedure have to be repeated for every important realignment of the laser system. In the second step a genetic algorithm finds the best actuators' configuration.

[2]The phase surface is measured by a 16×16 Shack-Hartmann analyzer.

The plane on the beam path that is conjugated to the Shack-Hartmann (SH) and the deformable mirror is situated right after the beam compressor. There are some $10m$ of free propagation between this plane and the point where beam is focused on the target. This fact limits the efficacy of the active correction by the DM and does not consider any of the forthcoming optics.

6.2 The experimental installation

The experimental setup provides *(i)* the optics to transport and focus the big, high power, beam, *(ii)* the optical diagnostics for the positioning of the target and *(iii)* the devices related to the ion beam. In Fig.6.6 the general scheme of the installation is presented.

1. Pump beam
2. Probe beam
3. Parabola
4. Target Holder
5. Microscopy of the focal spot (removable)
6. High magnification reference of target focus
7. Motorized delay line
8. (**a-c**) Thomson parabola and MCP
9. Transparency microscopy of the target (removable)
10. Lead screen and motorized image plate

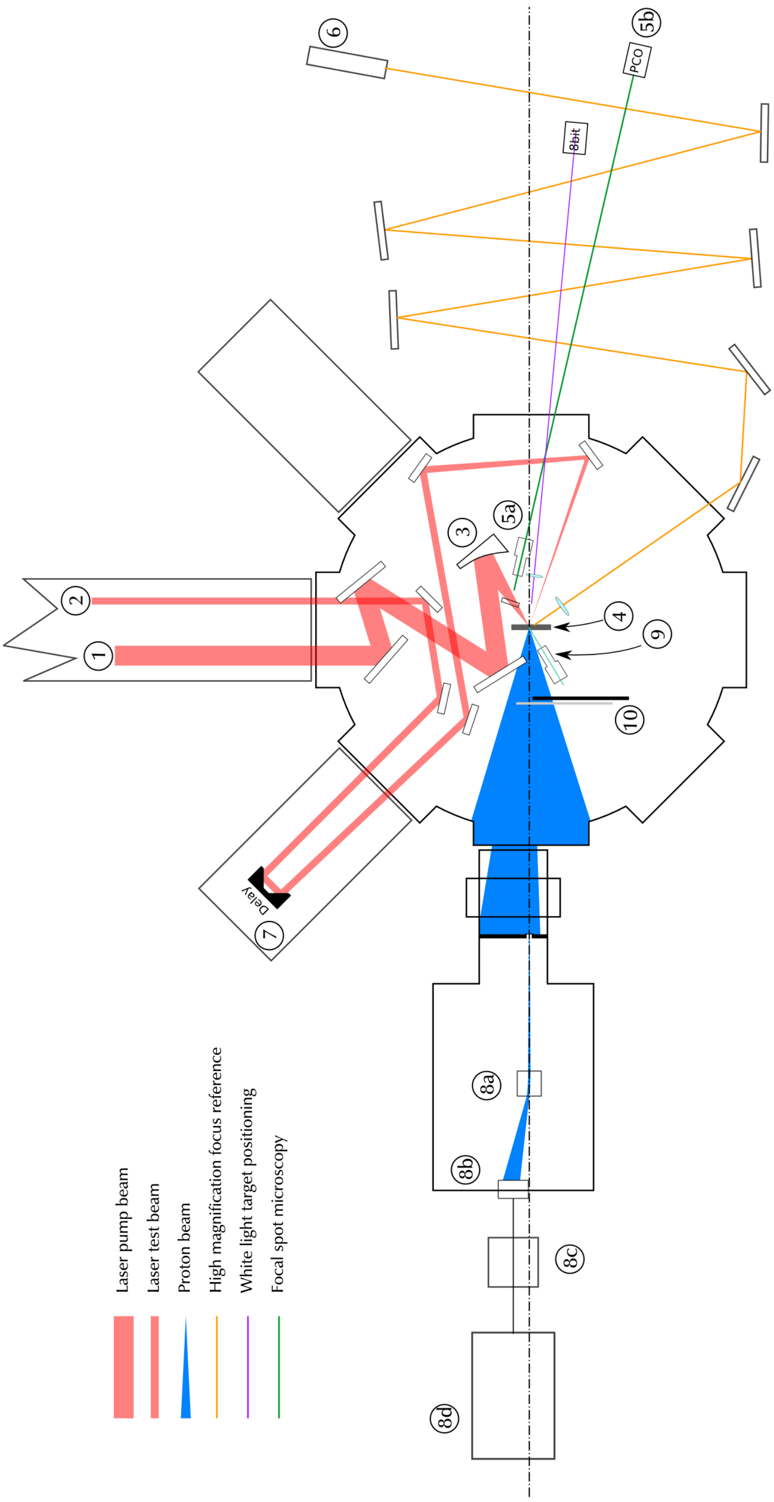

Figure 6.6: Scheme of the setup for laser-ion acceleration.

6.2.1 Laser Diagnostics

Energy

The laser in its present conditions produces $1.5J$ to $2J$ per pulse before compression. The optics chain from the source to the experimental installation transports a total of 37% (measured) in energy. The efficiency of the compressor alone accounts for $\approx 45\%$ of losses, which leaves $\approx 3\%$ loss for each mirror. At the end of the experiment the total transport coefficient decreased to 30%, probably due to aluminum deposition on the mirrors.

Focusing

The main beam is focused by a glass parabolic reflector; the parabola is a 30° off-axis cut, with a numerical aperture of $f/3$ and a focal length of $15cm$. The glass surface is gold coated to optimize the reflectivity. In the case of an ideal gaussian beam, the pump would be focused down to a waist of $w_0 = 1.4\mu m$.
To image the focal spot, the focused beam is intercepted by a removable mirror and sent through a microscope objective to a linearized camera (Fig.6.6-5). The quality of the spot is defined by measuring its transverse size and the ratio of energy contained in its $1/e^2$ contour (Fig.6.7).

Monitor of Laser Parameters

In a laser system of this size it is common to observe fluctuations in the functional parameters. A precise control of shot to shot behaviour is even more important in experiments where a single measurement cannot be repeated a number of times sufficiently high to authorize a statistical treatment. Nevertheless a strong correlation between the different parameters (energy, direction of the beam, contrast, etc.) is observed; this enables us to limit our observation of the laser status to some key parameters and be able to set a rejection criterion out of them.

During the experimental procedures, two diagnostics constantly keep the laser status under control: the pulse integrated energy and the contrast ratio.
The energy is integrated by a linearized camera: the small leak ($< 0.01\%$ of energy) from a dielectric mirror is enough to record the transverse profile of the beam and to

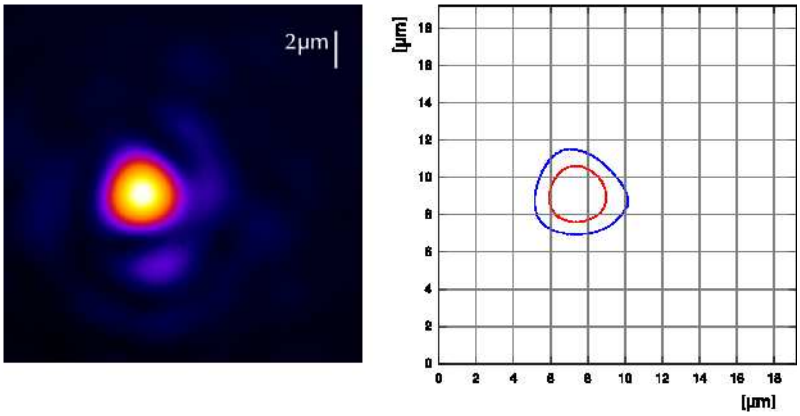

Figure 6.7: Laser focal spot at $800nm$; (a) image of the spot as seen by camera (resolution: $0.040\mu m/pix$, magnification: $230\times$); (b) contour plots of two different levels of intensity; in red the FWHM contour (diameters: vertical $2.92\mu m$, horizontal $3\mu m$); blue is $1/e^2$ (diameters: vertical $4.4\mu m$, horizontal $5\mu m$) which corresponds to an average waist of $2.35\mu m$. In the depicted case, a total of 72% of the energy is contained in the πw_0^2 surface.

observe the variation in energy. Two effects have been noticed in time: *(i)* a strong shot to shot and *(ii)* a slow drift on the average energy (Fig.6.8).

To measure the contrast of the pulse, an aluminum-coated glass blade is used to inter-

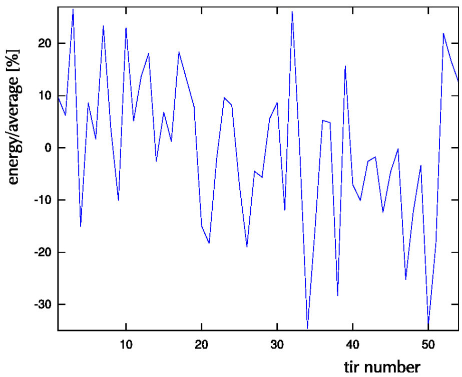

Figure 6.8: Typical shot-to-shot behaviour of integrated laser energy during 54 shots in a row; the peak-to-valley is as large as 60%.

cept a tiny part (smaller than $5mm^2$) of the main beam. The reflection is sent to a fast photocathode (rise time $< 500ps$) that is controlled by a fast oscilloscope. A number of neutral optical densities, enough to observe the peak of the femtosecond pulse, is added. Once the reference is taken, all of the densities are removed and the pedestal observed. The contrast is calculated from the ratio between the peak and the pedestal, taking in account the number of densities and the integration factor of the photocathode ($500ps/30fs = 1.6 \times 10^4$). The insertion of the blade did not produce any measurable worsening of the focal spot.

Target Positioning

The Rayleigh range of a gaussian beam with a waist of $2.3\mu m$ is $z_0 = \pi w_0^2/\lambda = 20\mu m$ which sets the scale of precision that is needed to align the target. Moreover, a precise absolute reference is important to ensure repeatability and meaningful comparison among different shots. The technique I find to work best is the collection of a part of the light that, from an Helium-Neon laser collinear to the main IR beam, is diffused by the rough target surface. A small lens images the helium-neon spot to a camera (Fig.6.6-6): the lens is aligned to provide a very big magnification ($\approx \times 50$), that is enough to map a range of $50\mu m$ of movement in target focus to the entire chip of an 8bit CCD camera. A small aperture lens is found to work better, for its small level of detail produces a cleaner spot, which eases the reference. I estimate the error on target positioning to be smaller than $15\mu m$.

6.2.2 Proton Diagnostics

Besides of the widely used CR39 or RCF plastics for ion dose integration, new systems are earning importance in the community of laser-ion accelerators, following the need of diagnostics that would produce experimental information in real time, or short time after. This possibility dramatically increases the efficiency of proton acceleration experiments, where some parameters need a direct feedback from the produced beam (the best example being the search of the correct focus position).

New technologies include image plates, scintillating materials and micro-channel plates. During this experiment, the main interest has been focused on the MCP plates, for their sensitivity, the resolution and the real-time availability of the experimental information. Image plates have been used to record the propagation direction of the beam as well as its divergence (see Fig.6.9).

CR39

The CR39 (California Resin-39[3]) is a plastic that is widely used as an ion dose integrator. Its chemical properties are modified by the energy deposition by massive particles traversing its bulk. The used reaction is the increased solubility of molecular fragments in a strongly basic environment[4]. The trajectory of a single particle continuously deposits energy while passing through the solid and no apparent damage is produced. When the surface is etched by a *base*, the volume that experienced radiation damage is corroded faster and holes are produced. Precise calibrations exists to correlate energies and species to the time evolution and the geometrical properties of the produced holes[85]. A simpler approach for spectral characterization of ion beam is obtained by superposing foils of increasing thickness on the detecting slab, to set lower cutoffs on measurable energies. The stopping power of filters can be calculated very precisely, letting to correlate the presence of radiation damage to a well defined energy range.

At the time of writing, no laser effect on CR39 is documented in the literature. I observed a threshold of about $10^{14} W/cm^2$ at $\lambda = 800nm$ to produce on the detector a type of impact absolutely similar to the signal produced by ions. No ablation is produced, and latent tracks appears only upon etching. To avoid the phenomenon it is necessary to protect the dose integrator from intense IR light. During the experiment, at least one non transparent (metallic) filter is put on the foil.

Image Plate

An alternative way for measuring the ion beam profile or the ion spectra is the use of Image Plates. Here a thick plastic foil is covered by a material that is characterized by very long lived molecular meta-levels. The transition from the ground state to a charged state is triggered by the deposition of energy by any kind of ionizing radiation. The material relaxation can happen spontaneously or be stimulated by electromagnetic wave with the proper wavelength, and results in the emission of photons. In a special scanner, the micrometric laser spot from a diode is used to stimulate this emission. The produced signal is read by a photomultiplier tube and digitized, to produce an image. The image resolution is theoretically limited only by the waist of the scanning laser beam which is, for our scanner, $25\mu m$. Some images we realized by exposing the plate

[3] namely *Polyallyl-diglycol-carbonate,* $C_{12}H_{18}O_7$.

[4] The reaction is usually accelerated by heating the bath; the most commonly used bases are the strongest ones, $NaOH$ and KOH. For a deeper insight in the etching process, see [85].

to a radioactive source (^{241}Am, $19kBq$) showed a bigger size for single impact (at least three times) which suggest a worse limit on the spatial resolution.
The foils are erased when exposed to incoherent white light for a certain time ($\approx 10-15$ minutes); they can be re-used afterwards.

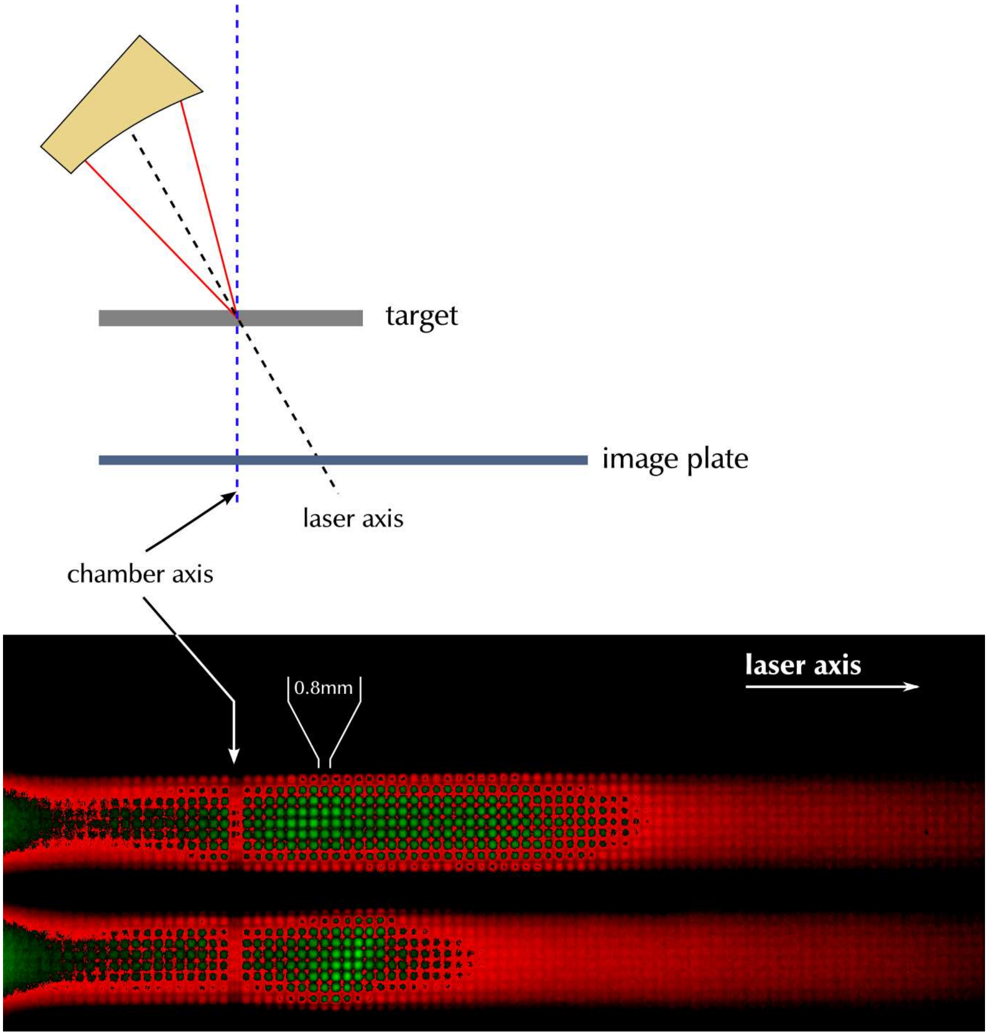

Figure 6.9: Example of use of an image plate to monitor the proton beam direction. The image, in fake colors, shows two shots where the proton axis is moving away from the main axis of the chamber, where the MCP is aligned. A filter of constant thickness composed by $200\mu m$ Mylar and $36\mu m$ Aluminum (total stopping power: $4.8MeV$) is used to cut lower energies, a steel grid of $0.8mm$ spacing to record the scale and a $200\mu m$ thick Aluminum wire is aligned on the MCP proton axis. The distance between the target and the IP is $12cm$; the figure shows the beam whose center travels at $3.5°$ from the MCP direction. The half-divergence for the over-threshold beams in the tracks is $\sim 7°$.

The resolution, the size of the active area (standard plates are sold in foil of $20\times 25cm$) and the ease of digitizing the integrated dose make this kind of detector very useful. The main problem is that they are sensitive to every kind of ionizing radiation of sufficient energy, which limits the possibility of using them in environments were e^- and γs are also present. To be able to discriminate between electrons and ions, I use a dual thickness filter, where a thicker one filters out all of the ion signal and the thinner sets a meaningful cutoff for the searched proton energies. The proton signal is obtained by direct subtraction between the two areas, from the assumption that the thicker filter ($\approx 500\mu m$ Mylar) would very slightly affect the signal from electrons and γs.

In our experiment we used IPs to image the propagation direction and the divergence of the generated proton beam, to ensure the proper alignment of other diagnostics (see later). For this purpose, the IP is positioned normal to the main axis of the chamber and covering with its active surface the space from the target normal to the prolongation of the laser axis (see Fig.6.6-10). The IP can be moved in the vertical direction. Two lead plates limit the exposed area to an horizontal stripe of $\sim 0.7cm$, which makes possible to use the same plate for several laser shots (Fig.6.9).

MCP and Thomson parabola

The main diagnostic system for real time detection of the products of the interaction is a Micro Channel Plate (MCP, Fig.6.6-b) coupled to a Thomson parabola (TP, Fig.6.6-a). A Thomson parabola is a device where an electric and a magnetic field are superposed, one parallel to the other; when a charged particle propagates through the region, two separate motions are set in place, due to the independent action of the two fields, and the particle is deviated according to its mass and charge. The Micro Channel Plate (MCP) (Fig.6.10) can be seen as an array of very high gain amplifiers. A strong electric signal is produced whenever a particle deposits energy on the surface. In the two following sections I analyze the theory of propagation in the TP and the experimental realization of the MCP+TP based detector for the ion acceleration experiment.

Theory The equations of propagation at non-relativistic energies for the generic ion of mass m and charge q in E, B fields like those defined in Fig.6.11 is

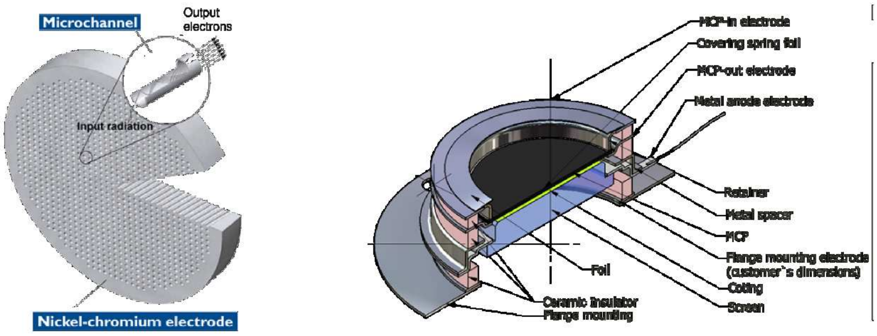

Figure 6.10: Graphical representation of the MC plate (left) and of its assembly (right).

$$\begin{cases} x\,(t) &=& \dfrac{1}{2}\dfrac{qE}{m}t^2 \\ \\ y\,(t) &=& R\,[1-\cos\left(\omega_c t\right)] \\ \\ z\,(t) &=& R\sin\left(\omega_c t\right) \end{cases} \tag{6.2}$$

where $\omega_c = qB/m$ is the common cyclotron frequency and $R = v_0/\omega_c$. Following the depicted geometry, the particle is supposed to have $v_0 = v_{0,z}$. The magnetic term in the Lorentz force $\underline{\mathrm{v}} \times \underline{\mathrm{B}}$ is perpendicular to $\underline{\mathrm{E}}$, so the two motions, electric and magnetic, are independent one to the other. The only interaction between the two motions happens due to the finite size of the field region; the interaction with the electric field produces an acceleration of the particle, making a term in v_x to appear. The final value of v_x depends also on the time needed to the particle to exit the area of influence, which is longer than what it would be observed without a B field, for the circular trajectory in the $z-y$ plane. In the simplified case of $L_B = L_E$ (the lengths of the field regions on the $z-$axis), according to (6.2)$-2,3$ the time needed to reach the end of the TP is

$$t_B = \frac{1}{\omega_c}\arcsin\left(\frac{L_B}{R}\right) \tag{6.3}$$

from which on the plane $(x, y, z = L_B) = (x_S, y_S)$ it holds

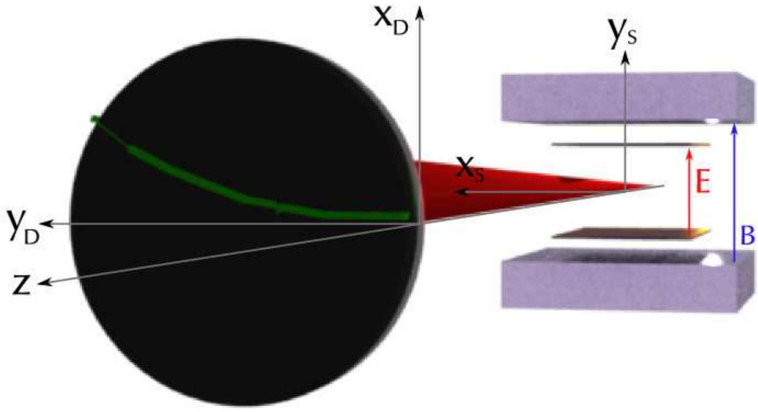

Figure 6.11: Graphical representation of the realized device (Thomson parabola and MCP).

$$\begin{cases} x_S &= \dfrac{1}{2}\dfrac{qE}{m\omega_c^2}\arccos\left(1-\dfrac{L_B}{R}\right)^2 \\ \\ y_S &= R\cdot\left[1-\left(1-\dfrac{L_B^2}{R^2}\right)^{1/2}\right]. \end{cases}$$

The exit angles are calculated through $\theta_x = \arctan(v_x/v_z)$ on the x projection and from simple geometrical considerations for the y projection. It gives

$$\begin{cases} \theta_x &= \arctan\left[\left(\dfrac{qE}{m}t_B\right)\cdot\left(R\omega_c\sin(\omega_c t_B)\right)^{-1}\right] \\ \\ \theta_y &= \arcsin\left(\dfrac{L_B}{R}\right). \end{cases}$$

The coordinates on the detector plane $(x_D, y_D) = (x, y, z = L_D)$, where L_D is the distance from the detector plane and the TP entry point $(0,0)$, are calculated through

$$\begin{cases} x_D &= x_S + (L_D - L_B)\tan(\theta_x) \\ \\ y_D &= y_S + (L_D - L_B)\tan(\theta_y) \\ &= y_S + \frac{L_B/R}{\left(1-L_B^2/R^2\right)^{1/2}} \,. \end{cases} \tag{6.4}$$

Experiment The detector is an array of a *(i)* micro channel plate (MCP, Fig.6.6-b-upper), *(ii)* a phosphor screen (Fig.6.6-b-lower) and *(iii)* a camera (Fig.6.6-d).
The MCP plate is a matrix of hollow glass capillaries ($\phi = 8\mu m$) whose internal walls are coated with a material with a very low work potential. Two electrodes are placed on the entrance and the exit surface of the matrix, to maintain an electrostatic field at a small angle[5] from the channel direction. When an electron set free from the electrode at the entrance, it drifts through the channel; secondary electrons are produced and made drifting upon collisions on the channel walls. The resulting charge distribution at the exit surface keeps in the amount of extracted charge, the relative distribution of energy that was deposited at the entrance. The emerging electron cloud is made drifting by the second electric field, until it impacts on the phosphor screen. In this way, an image on the phosphor screen reproduces the dose distribution that impacted on the plate. From this point of view, the MCP can be regarded as an imaging device, as the spatial information is not discarded in the amplification process.

Our setup uses a stack of two coupled channel plates (Chevron) to enhance the amplification factor. Typical high-voltage values are $-1.2kV$ on the MCP and $+4kV$ on the phosphor (see Fig.6.13 for schematics). To be able to raise the MCP to $1.2kV$ is necessary to isolate the vacuum gauge from the volume were the channel plate sits, as the weak ion signal produced by the cold cathode is strong enough to generate a high rate of random counts. In the MCP chamber a metallic grid, set to fixed potential of $30V$ to the chamber earth, is used for this purpose. Even if a maximum of $2kV$ is allowed ($1kV$ per plate), voltages higher than $1.3kV$ enormously increase the dark current signal, producing a strong fluorescence on the phosphor.
The final setup is mounted in a separate volume which is connected to the main interaction chamber by a $200\mu m$ pinhole[6]. This is set to fix the resolution of the spectrometer and to produce a differential vacuum between the two volumes; the MCP has to sit in

[5]This is a structural parameter of the MCP. Typical values range from 5° to 12°.

[6]The pinhole is realized on a $2mm$ thick lead plate which is screwed on a $\phi = 1mm$ aperture on the vacuum flange behind the vacuum gate (Fig.6.13). The coupling between the plate and the flange is vacuum tight, for a circular blade on the flange surface enters the lead bulk.

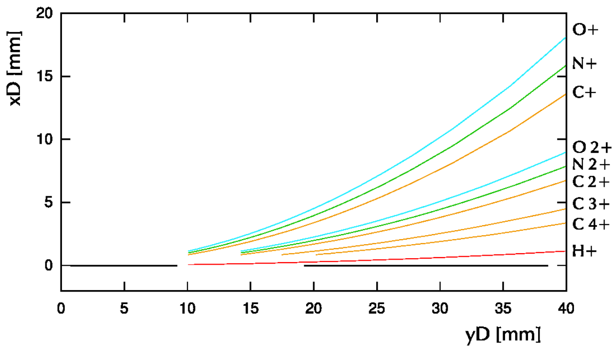

Figure 6.12: Distribution of protons and different ionization degrees for atoms of carbon, oxygen and nitrogen on the MCP plane (Numerical simulation. Magnetic field is experimentally mapped, Fig.6.14. Electric field is set to $E = 2.5 \times 10^5\, V/m$ for $L_E = 4cm$).

a vacuum better than $10^{-5} mbar$ when high voltage is applied.

The pinhole is situated at a distance of $80cm$ from the interaction point. This parameter is very important, as it sets the divergence of the analysed beam and the maximum error that is allowed while aligning the target tilt, in order not to miss the main beam (see 6.2.1). The phosphor window is imaged through a photographic objective (Fig.6.6-8c) on a $16bit$ intensified camera. The final recorded image has a resolution of $44.29 \mu m/pix$.

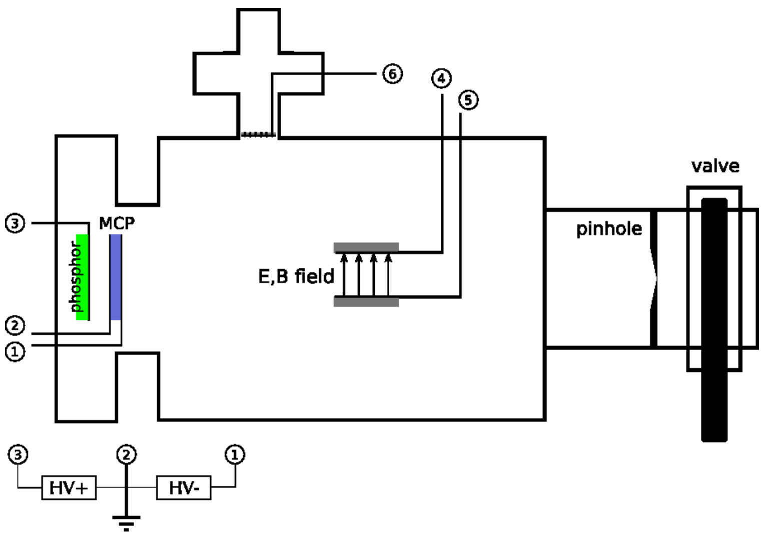

Figure 6.13: Schematics of the TP+MCP chamber (1)-(2) electrodes for MCP polarization; (3) phosphor input electrode; (4)-(5) electrodes for TP electric field; (6) shielding gate

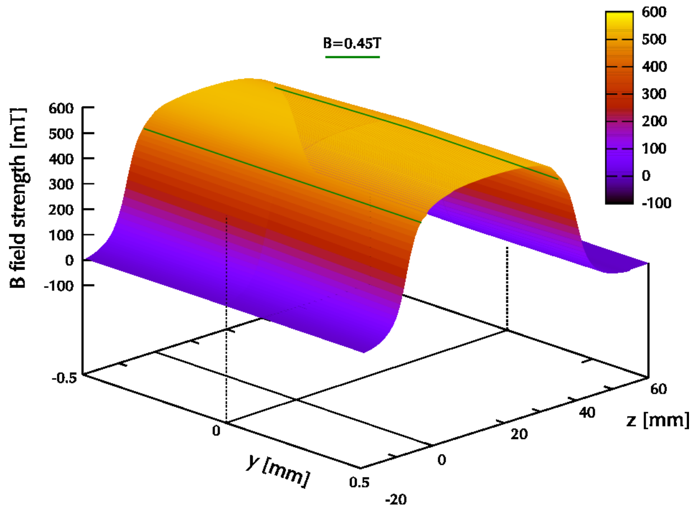

Figure 6.14: Map of the magnetic field strength on the plane $x = 0$. Important fringe field is found, which makes necessary the use of the map in numerical simulations for the calibration of the Thomson parabola.

To analyze consistently the spectral tracks from the MCP, the absolute reference of the spectrometer axis has to be set on the images. The axis is the prolongation of the chamber axis that is pictured in Fig.6.6, defined by the axis between the interaction point and the pinhole. The experimental procedure to observe this point uses the acceleration of non-ionized atoms and molecules from the Aluminum target. When shooting with a strongly attenuated laser (we used 1% of fully amplified power, $I_0 \sim 10^{17}\, W/cm^2$) no ion acceleration exists, though the intense heating of the metal foils produces evaporation. Neutral atoms are spread in the vacuum and their impact on the MCP plate is sufficient to produce a signal on the camera. Since their trajectories are not affected by the E, B fields, the impact point marks the acceleration axis.

During the full power shots, the area of the MCP that lies on the neutral axis has to be shielded[7], for the large quantity of debris that is produced during the interaction strongly saturates both the channel plate and the recording camera; such an electronic signal forms a halo on important part of the recorded image.

[7] I used a $3mm$ thick Plexiglas plate.

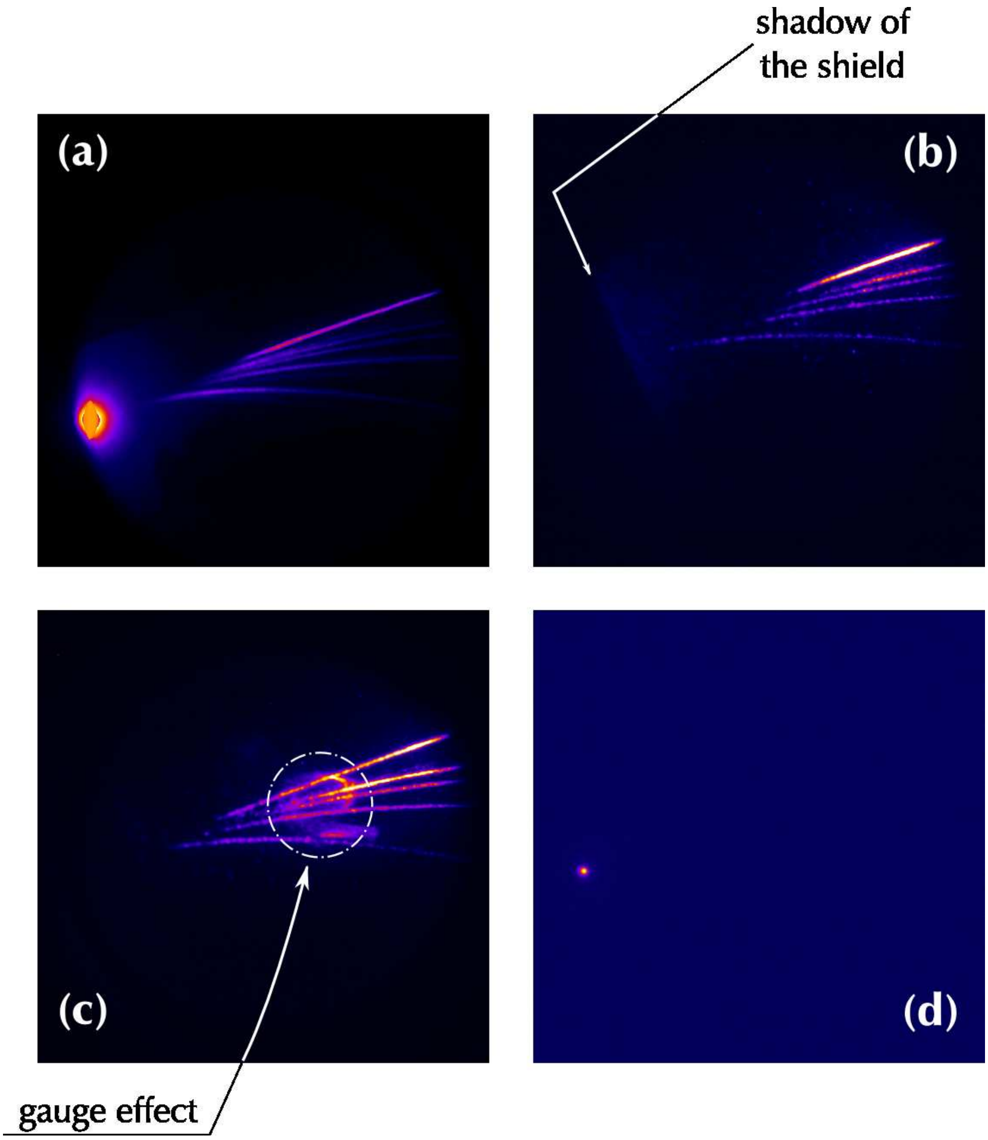

Figure 6.15: Examples of images recorded from the MCP: (a/b) unshielded and shielded zero; (c) effect of gauge ions at high MCP voltage; (d) zero point reference taken at low laser power.

Numerical treatment of images Once the image is recorded, its analysis is done in two steps: *(i)* a numerical integration, to get an histogram from every single track and *(ii)* the inversion of the simulated dispersion curves to define the energy scale.

The numerical integration is necessary to produce an histogram where the position and

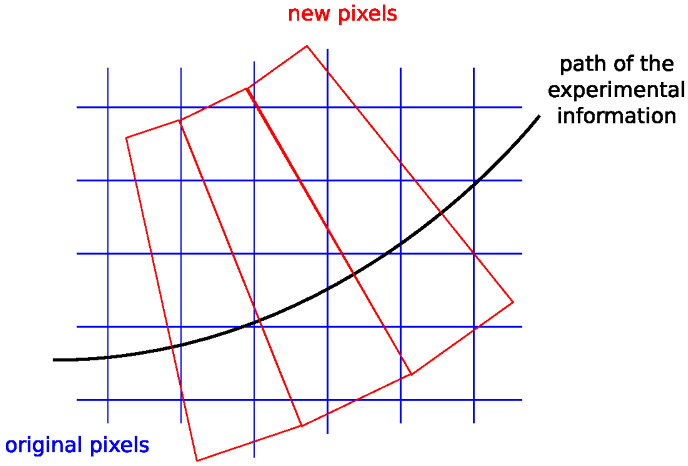

Figure 6.16: Strategy of analysis for the proton/ion tracks on the channel plate: the new histogram is built along the physically meaningful direction and super-pixels boundaries are defined; the count associated on a super-pixel comes from the partial integrals of the underlying histogram, defined by counts on the camera pixels.

the shape of bins is physically meaningful. For example, to analyse the component of the dispersion in energy due to the magnetic field, where the contained physical information is sufficient to obtain the energy spectrum, the bins have to refer, in distance, to a precise dispersion direction, which is not horizontal in the camera frame. The problem is resolved defining a set of super-pixels (marked in red in Fig.6.16) with a different geometry on the image and to associate them a certain number of counts. Assuming the count on each pixel from the original image to be uniformly spread on area, the count for a super pixel is calculated by integrating the underlying counts. The quantities are multiplied by a geometrical weight factor which equals to 1 for those entirely contained and to the surface fraction for the partially contained ones. For a given set of super pixels, the map of geometrical weights is calculated by Montecarlo integration of the two geometries. This is most important when the super pixel size becomes comparable to pixel size (Fig.6.16).